Process-structure-property modelling for post-build heat treatment of powder bed fusion Ti-6Al-4V

Jianxin Liu [a,b,1], *Xinyu Yang* [c,1], *Xingzai Chai* [a,b], *Adrian Boccardo* [d,e,f], *Yefeng Chen* [a,b], *Xiaowei Wang* [a,b], *Seán B. Leen* [d,e,*], *Jianming Gong* [a,b*]

[a] *School of Mechanical and Power Engineering, Nanjing Tech University, China*

[b] *Jiangsu Key Lab of Design and Manufacture of Extreme Pressure Equipment, Nanjing, China*

[c] *Institute of High Performance Computing (IHPC), Agency for Science, Technology and Research (A*STAR), 1 Fusionopolis Way, #16-16 Connexis, Singapore 138632, Republic of Singapore*

[d] *I-Form, the SFI Research Centre for Advanced Manufacturing, Ireland*

[e] *Mechanical Engineering, School of Engineering, College of Science and Engineering, University of Galway, Ireland*

[f] *IMDEA Materials Institute, Madrid, Spain*

[1]*These authors contributed equally to the work.*

Abstract

Post-build heat treatment is an important component in optimized manufacturing processing for laser beam powder bed fusion (PBF-LB) Ti-6Al-4V. The development of predictive modelling, based on the understanding of the relationships between process parameters, microstructure evolution and mechanical properties, is a potentially key ingredient in this optimization process. In this paper, a process-structure-property (PSP) model is developed to predict the effect of post-build heat treatment on yield strength, which is a key tensile property for PBF-LB Ti-6Al-4V. The process-structure part is developed with a focus on the prediction of solid-state phase transformation, especially dissolution of martensite during the heating phase. Subsequent tensile properties are quantified by a microstructure-sensitive yield strength model based on the predicted microstructure variables. The integrated PSP model is validated by via experimentally measured phase fraction, α lath width and monotonic tensile tests on PBF-LB Ti-6Al-4V with different heat-treatment temperatures, for identification of optimal process parameters.

Keywords: Laser beam powder bed fusion; Ti-6Al-4V; Solid-state phase transformation; Yield

∗ Corresponding authors.

E-mail address: sean.leen@universityofgalway.ie (S. Leen), gongjm@njtech.edu.cn (J. Gong)

strength; Heat treatment

1. Introduction

In recent years, laser beam powder bed fusion (PBF-LB) has become one of the most widely used methods in additive manufacturing (AM), and has been adopted to manufacture numerous strategically-important products with complex geometries. Typical materials include stainless steel, titanium and aluminum [1]. PBF-LB Ti-6Al-4V is one of the most strategically important due to its wide usage in critical industry applications, including biomedical and aerospace. Conventional Ti-6Al-4V has two main crystal structures: hexagonal close-packed structure (HCP) α-phase and body-centered cubic (BCC) β-phase. In contrast with conventional Ti-6Al-4V, PBF-LB Ti-6Al-4V has a predominantly martensitic microstructure (α′-phase, >95% [2], also HCP), attributed to the rapid cooling process after heating in PBF-LB, which is stronger but more brittle than typical α-phase [3]. Due to the characteristics of martensite, as-built PBF-LB Ti-6Al-4V shows enhanced strength but significantly poorer ductility (elongation normally < 10% [4]). Thus, post-heat treatment for optimization of strength-ductility properties of Ti-6Al-4V is necessary.

It has been reported that α, β and α′ phase fractions can be controlled by solid-state phase transformation (SSPT) during different heat treatment processes [3, 5]. Moreover, since different phases dominate different mechanical properties, e.g. acicular α′ martensite usually exhibits high strength and low ductility, β-phase gives the opposite and α-phase is in between [3, 6-9], the mechanical properties of PBF-LB Ti-6Al-4V can potentially be tailored by tuning the post-heat treatment process. Vrancken et al. [3] found that heat treatment below the β transus temperature can transform α′ martensite into lamellar α+β structure with retained columnar features of prior β. Higher heat treatment temperature also results in coarsening of α-phase and higher volume fraction of β-phase. In addition, columnar-to-equiaxed transition of prior β grains occurs when the temperature is above β transus. The effect of different cooling rates on the microstructure of Ti-6Al-4V has been extensively studied [10-15]. When the cooling rate is lower than 20 ℃/s, diffusion-controlled β to α phase transformation occurs with clear prior β grain boundary. Most of the α phase nucleates non-uniformly at the prior β grain boundary and grows into the grain interior. For intermediate cooling rates, e.g. 20 to 410 ℃/s, diffusion-less phase transformation (i.e. martensitic transformation, β to α′) is accompanied by the diffusion-controlled process. Martensitic transformation dominates the SSPT process when the

cooling rate is higher than 410 ℃/s, in which case a hexagonal microstructure of acicular α′ martensite forms from the lattice shear of β phase accompanied with the broken and annihilation of prior β grain boundary.

Different phase composition due to different heat treatment processes have a significant effect on the tensile properties of treated samples. Vranchen et al. [3] showed that the ductility of heat-treated PBF-LB Ti-6Al-4V specimens increased to 12.8% after post-build heat treatment at 850°C for 2 h followed by furnace cooling, which represents an increase of 74% relative to the as-built specimens. Zhang et al. [16] annealed PBF-LB Ti-6Al-4V at different temperatures from 600 °C to 900 °C for 2 h. Corresponding results show that ductility to the level of the forged Ti-6Al-4V can be obtained at the cost of reduced strength for the samples treated at temperatures larger than 850 °C. In addition, superior tensile properties of heat-treated PBF-LB Ti-6Al-4V compared to conventional Ti-6Al-4V can be achieved. Charlotte et al. [17] simultaneously improved strength and ductility of PBF-LB Ti-6Al-4V specimens by generating an α+α′ dual-phase microstructure with significant work hardening behavior through post heat-treatment between 850 and 920 °C. For example, the specimens heat treated at 920 °C, containing 51% of martensite, show 13% increment on both ultimate tensile strength and uniform engineering strain comparing to those of a wrought Ti–6Al–4V. Thus, the tensile properties of treated PBF-LB Ti-6Al-4V can be tailored by controlling the α/α′ phase ratio. Although α′ martensite can be fully transformed to Widmanstätten α (α_w) by a specific post-build heat treatment process to obtain better ductility, the material strength is concomitantly also significantly reduced. Retained α′ martensite can still contribute to the relatively high strength while the transformed α_w improves the poor ductility of as-built PBF-LB Ti-6Al-4V. It has been reported that the combined optimal strength-ductility properties can be achieved by generated a lamellar α+β structure via annealing treatment of PBF-LB Ti-6Al-4V [18].

Although the post-build heat treatment of PBF-LB Ti-6Al-4V has been extensively studied, most studies use a trial-and-error approach to optimize heat-treatment parameters. The development of an integrated process-structure-property (PSP) model has the potential to make this optimization process more efficient and objective. In general, PSP model development can be divided into process-structure model development and structure-property model development. The process-structure model aims to obtain microstructure variables which have deterministic effects on the tensile

properties, such as phase fractions and grain size. Full-field microstructural models, e.g. phase field and cellular automaton (CA) methods, can provide detailed phase information such as phase fraction evolution, spatial distribution and phase morphology. For example, Sahoo et al. [19] successfully simulated the columnar structure of PBF-LB Ti-6Al-4V which consists of prior β boundary and α grains using phase field simulation. In terms of CA methods, Zinovieva et al. [20] reproduced the experimental grain structures of PBF-LB Ti-6Al-4V considering multi-track and layer-by-layer processes. De Baere et al. [21] studied the SSPT evolution of PBF-LB Ti-6Al-4V during the post-heat treatment above the β transus temperature and the predictions were also validated by experimental observations. However, such simulations have very high associated computational expense, particularly given the small scale of material typically modelled. Mean-field models, for example the classical Johnson-Mehl-Avrami-Kolmogorov (JMAK) model, have been adopted to predict the phase fractions with acceptable accuracy. In our recent work, a modified incremental form of the JMAK model is proposed to predict phase evolution during the non-isothermal processes associated with PBF-LB [22]. In addition, α lath width as a key microstructure variable is also predicted, with the aim to establish the linkage between strength and microstructural features [23]. Structure-property models are usually developed to capture the microstructure-sensitivity of PBF-LB material [24, 25]. Specifically, full-field crystal plasticity (CP) model, e.g. crystal plasticity finite element (CPFE) [26-28] and crystal plasticity fast Fourier transform (CPFFT) [29-31] models, are widely used to predict mechanical properties based on inherited microstructure, e.g. from the PBF-LB process. However, the visible intra- and inter-granular mechanical fields from full-field CP also results in very high computational overhead and again, for a typically small-scale representative volume element (RVE) of simulated material. Classical Taylor-type modelling, although based on the iso-strain assumption and neglecting intergranular interactions, can provide efficient predictions, and have been enhanced with physically-based strengthening mechanisms, for microstructure effects, via incorporation of dislocation density evolution [32-34].

In this paper, the process-structure model [22] and structure-property model [24] from our previous work are integrated together in MATLAB, enabling implementation of an integrated PSP predictive capability, with extension to optimize the post-build heat treatment process. Specifically, as the thermal history of the heat treatment process is different from the PBF-LB process itself, in particular

with respect to a significantly lower cooling rate, corresponding cooling rate effects are captured in the present work to improve the prediction accuracy. Based on the predicted phase fractions, corresponding grain sizes for different phases are calculated. Thus, the microstructure-sensitive yield strength model proposed in our previous work [24] can be used to quantify the effects from different post-build heat treatment processes. The validity of the proposed PSP model is verified by metallographic observation and monotonic tensile testing.

2. Experimental methodology

In this study, aerosol-produced Ti-6Al-4V powder was used for PBF-LB processing, with the chemical composition listed in Table 1. Most of the powder particles are regular spheres with an average particle size of 45 μm, as shown in Figure 1. The PBF-LB process was carried out in an argon atmosphere using SLM®280 HL provided by SLM Solutions Group AG. The commercial standard process parameters (Table 2) were adopted with a preheating temperature of the substrate set at 200 ℃. The laser scanning strategy is shown in Figure 2. A 15° rotation of the scanning direction between successive layers was used. Both the process parameters and the scanning strategy are optimized parameters from SLM Solutions. In total, 25 cuboid specimens with length × width × height equal to 95 mm × 13 mm × 14 mm were manufactured. Since heat-treatment temperature has significant effects on microstructure and mechanical properties [35, 36], a wide range of holding temperatures is selected based on the schematic diagram of SSPT mechanisms (Figure 3) of PBF-LB Ti-6Al-4V. When the holding temperature is lower than the martensite dissolution temperature (M_D = 400 ℃ [37]), α′ martensite is retained with no SSPT. The α′ martensite partially dissolves to α and β when the holding temperature is between M_D and martensite start temperature (M_S = 575 ℃ [15]). Corresponding phase fractions are controlled by the equilibrium phase fraction, which is determined by the holding temperature. When the holding temperature is higher than M_S but lower than the β transus temperature (T_β = 994 ℃ [15]), the residual α′ fully transforms into α and β. Subsequent α to β transformation occurs simultaneously based on the specific ratios between equilibrium α and β phases. Full β phase is assumed once the holding temperature is between the range of T_β and liquidus temperature (T_L = 1655 ℃ [38]). During the slow cooling process, for example, subsequent furnace cooling in this heat-treatment study, β to α transformation can be observed until an equilibrium state is achieved. As such, it is clear that different holding temperatures, relative to phase transition temperatures, will result in different phase compositions. In order to obtain representative microstructures of PBF-LB Ti-6Al-4V after heat-treatment, corresponding holding temperatures are defined between 500 and 900 ℃ (i.e. 500, 600, 700, 750, 800, 850, 900 ℃). The as-printed cuboid specimens are removed from the substrate and then heat-treated in a TL2012 type muffle furnace based on the schematic shown in Figure 4. The heating rate is set as 5 ℃/min with a dwell time of 2 hours at the holding temperature. The cooling rate for furnace cooling is approximately 1 ℃/s.

Table 1. Chemical composition of the Ti-6Al-4V powder in wt.%. The balance is Ti.

Al	V	Fe	C	O	N	H	Mo	Cu	Ti
6.07	3.98	0.14	0.007	0.13	0.007	0.02	0.05	0.05	Bal

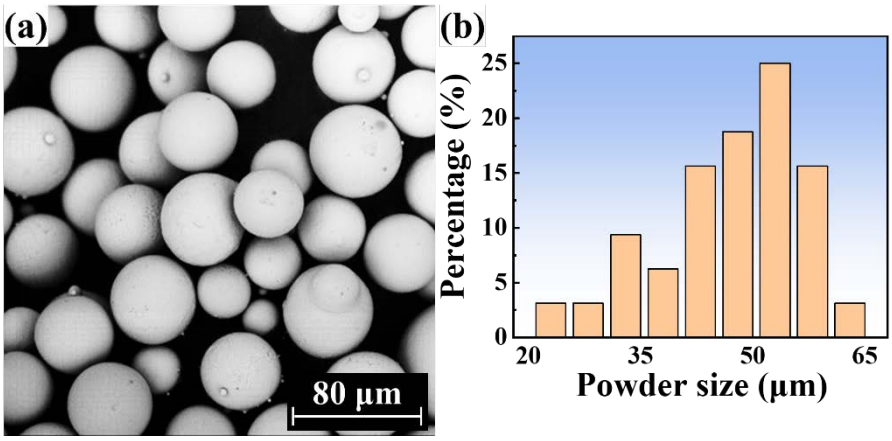

Figure 1. (a) Morphology of Ti-6Al-4V powder particles and (b) powder size distribution.

Table 2. Commercial standard process parameters of SLM®280 HL.

Laser power (W)	Scanning speed (mm/s)	Layer thickness (µm)	Hatching spacing (mm)
275	1100	30	0.12

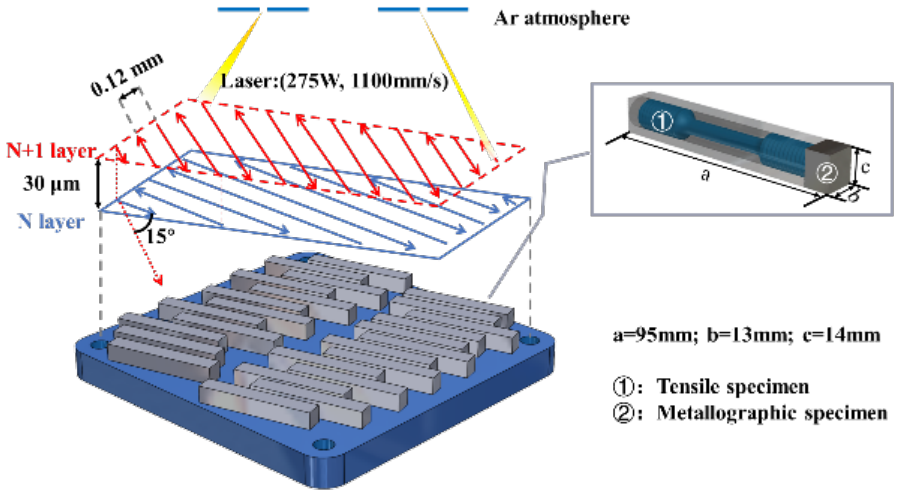

Figure 2. Schematic of laser scanning strategy in PBF-LB process and layout of cuboid specimens (95 mm × 13 mm × 14 mm). Each cuboid is further machined into a tensile test specimen and a metallographic specimen after the post-build heat treatment process.

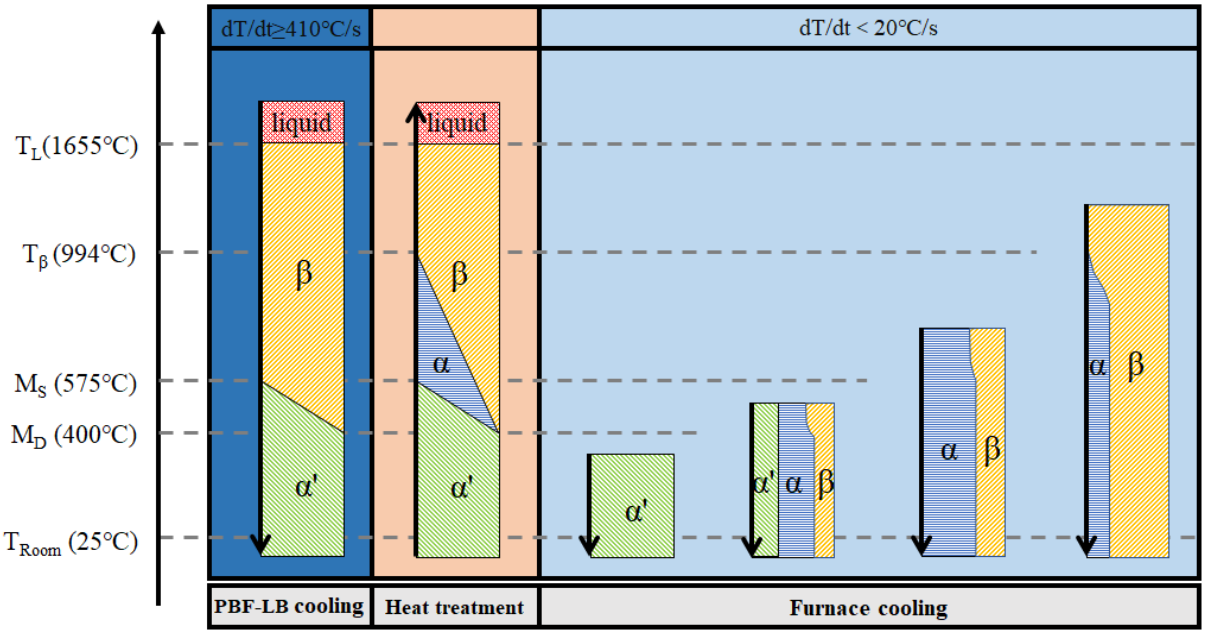

Figure 3. Schematic of SSPT mechanisms for PBF-LB Ti-6Al-4V at different holding temperatures and cooling rates [39].

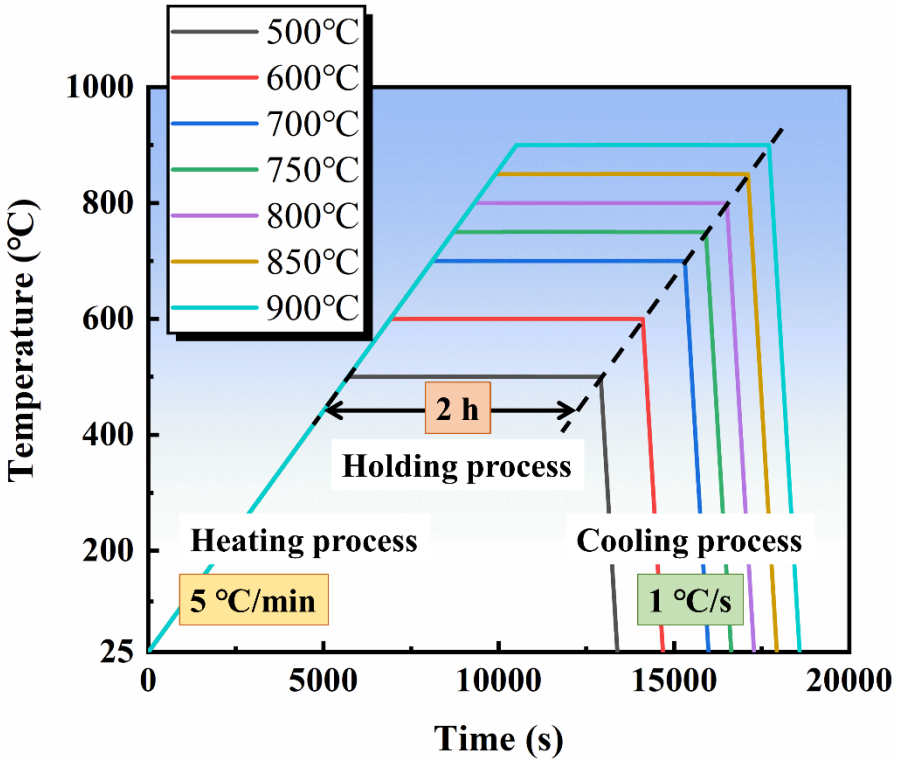

Figure 4. Schematic of heat-treatment processes at different holding temperatures with heating rate: 5 ℃/min, dwell time: 2h and cooling rate: 1 ℃/s.

After heat-treatment, as shown in Figure 2, 10 mm × 10 mm × 5 mm metallographic specimens were cut from the cuboids. The sample surface was polished using 2000# SiC sandpaper and roughly polished with a water-soluble polishing paste. In order to obtain a bright, scratch-free mirror surface, a metallographic spray polishing solution with a particle size of 0.5 μm was employed. The metallographic specimens were etched by a specific reagent with $HF:HNO_3:H_2O = 1:3:46$ [40] for about 18 s and immediately cleaned up. Optical microscopy (OM) and scanning electron microscopy (SEM) were used for microscopic observation and corresponding phase compositions were measured and calculated using the MIPAR software [41, 42]. In addition to the metallographic specimens, tensile specimens were also machined from the cuboid sample with a gauge length of 25 mm following ASTM E8/E8M-21 standard, as shown in Figure 5. Monotonic tensile tests were conducted at a strain rate of 1.0×10^{-3}/s, using a SINOTEST EQUIPMENT RPL-100 machine equipped with a 100 kN load cell.

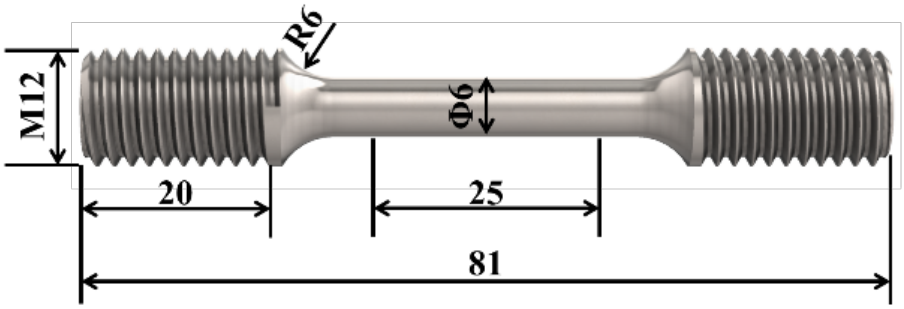

Figure 5. Geometry and dimensions of monotonic tensile test specimen.

3. Modelling framework

In this work, the integrated PSP model is developed by adapting and sequentially coupling our process-structure model [22] and our structure-property model [24], with specific modifications relating to the present heat treatment processes. Eq. (1) shows the classical JMAK model [43-46], which is usually used to describe a complete phase evolution from 0 to 100%:

$$F = 1 - e^{-k(t^{\mathrm{eq}})^n} \tag{1}$$

where F is the phase fraction, t^{eq} is the equilibrium time, k and n are kinetic parameters. In order to apply the JMAK model for incomplete phase transformation and non-isothermal conditions, an incremental form with different initial phase fractions can be expressed [47] as :

$$F_{\alpha,i} = \left[1 - e^{-k_i\left(t_i^{\mathrm{eq}} + \Delta t\right)^{n_i}}\right] \left(F_{\alpha,i}^{\mathrm{eq}}\right)\left(F_{\alpha,i-1} + F_{\beta,i-1}\right) \tag{2}$$

where the α phase fraction at time step i ($F_{\alpha,i}$) is determined by the α and β phases at the previous time step $(F_{\alpha,i-1} + F_{\beta,i-1})$ with updated kinetic parameters (k_i, n_i) and equilibrium time (t_i^{eq}) at successive temperatures. The various parameters can be inversely calculated based on published TTT (temperature-time-transformation) curves [22] and the calculated equilibrium α-phase fraction as a function of temperature is shown in Figure 6.

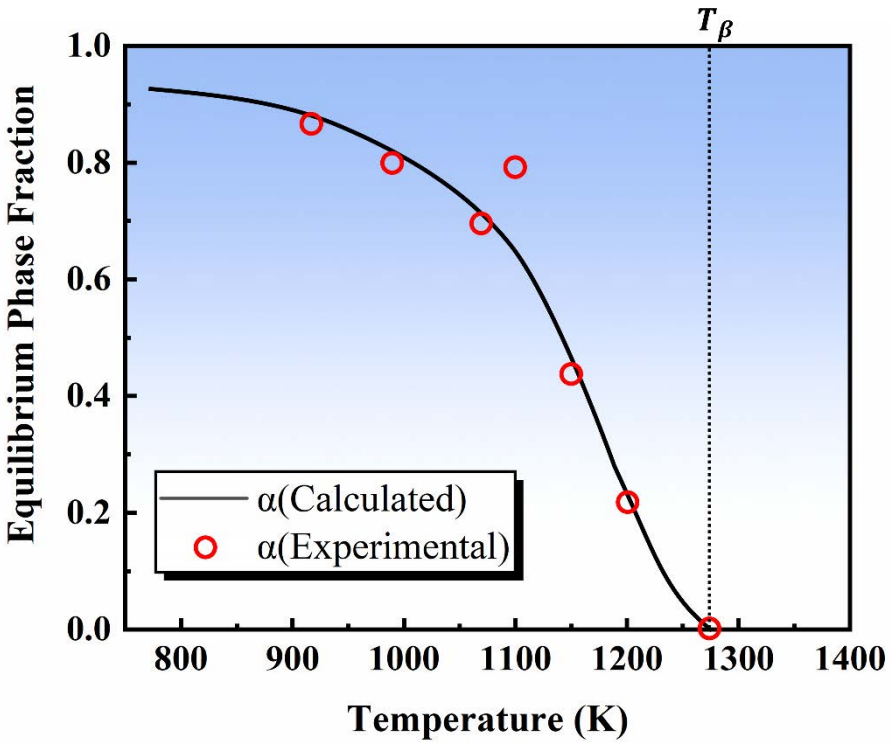

Figure 6. Calculated equilibrium α-phase fraction compared with experimental data [48].

Figure 7 shows a flowchart of the relevant SSPT mechanisms during post-build heat treatment of PBF-LB Ti-6Al-4V. α' martensite, which is the dominant microstructure (>95%) of as-built PBF-LB Ti-6Al-4V, is a non-equilibrium phase, attributed to the rapid cooling process, and it is stable at room temperature. During heating and holding periods of the heat treatment, the α′ martensite dissolves to a relatively stable α+β phase. Most of the α-phase is α_w and β-phase nucleates at the grain boundaries of α′ martensite [49]. The dissolution of α′ martensite is a diffusion-controlled phase transformation process [50] which can generally be described by Eqs. (3) to (5):

$$F_{\alpha\prime,i} = F_{\alpha\prime,i}^{\mathrm{eq}} - \left[e^{-k_{\alpha\prime,i}\left(t_{\alpha\prime,i}^{\mathrm{eq}}+\Delta t\right)^{n_{\alpha\prime,i}}}\right]\left(F_{\alpha\prime,i-1} + F_{\beta,i-1} - F_{\alpha\prime,i}^{\mathrm{eq}}\right) \quad (3)$$

$$F_{\alpha_w,i} = F_{\alpha_w,i-1} + \left(F_{\alpha\prime,i-1} - F_{\alpha\prime,i}\right)\left(F_{\alpha,i}^{\mathrm{eq}}\right) \quad (4)$$

$$F_{\beta,i} = F_{\beta,i-1} + \left(F_{\alpha\prime,i-1} - F_{\alpha\prime,i}\right)\left(F_{\beta,i}^{\mathrm{eq}}\right) \quad (5)$$

where the formed α_w and β is calculated based on the current equilibrium phase fractions. Kinetic parameters and equilibrium phase fractions for α′ martensite have been obtained from the work of Gil Mur et al. [37]. When the holding temperature is higher than M_S but lower than T_β, α_w further transforms to β-phase. The growth of β-phase is controlled by diffusion of vanadium and can be mathematically described as:

$$F_{\beta,i} = A(T)\sqrt{t} \tag{6}$$

where the diffusion rate $A(T)$ depends on holding temperature and is expressed in the form of parabolic rate [35]:

$$A(T) = a\left(\frac{T_i}{T_{\mathrm{ref}}}\right)^b \tag{7}$$

where T_i is current temperature in Kelvin with reference temperature T_{ref} = 1 K. Coefficients a = 2.2×10^{-31} $s^{-1/2}$ and b = 9.89 have been previously identified by Kelly et al. [35].

Compared with the PBF-LB process, furnace cooling during post-build heat treatment has a significantly lower cooling rate (<20℃/s) [9], leading to negligible formation of α′ martensite, as depicted by the continuous cooling transformation (CCT) curve of Figure 8. The diffusion-controlled phase transformations, i.e. β to α_{gb} (located at prior β grain boundary) and α_{w}, are dominant during such cooling periods. The use of the previous SSPT model [22] tends to numerically approach the equilibrium phase fraction, which is not consistent with experimental observations. Consequently, we have improved the iteration algorithm by combining the conventional JMAK solutions at two successive time steps to avoid overestimating phase transformations, as:

$$\begin{aligned} F_{\alpha_{\mathrm{gb}},i} &= \Delta F_{\alpha_{\mathrm{gb}},i-1} + F_{\alpha_{\mathrm{gb}},i-1} \\ &= \left[1 - e^{-k_{\alpha_{\mathrm{gb}},i}\left(t^{\mathrm{eq}}_{\alpha_{\mathrm{gb}},i}+\Delta t\right)^{n_{\alpha_{\mathrm{gb}},i}}}\right]\left(F^{\mathrm{eq}}_{\alpha,i}\right)\left(F_{\beta,i-1}\right) \\ &\quad - \left[1 - e^{-k_{\alpha_{\mathrm{gb}},i-1}\left(t^{\mathrm{eq}}_{\alpha_{\mathrm{gb}},i-1}+\Delta t\right)^{n_{\alpha_{\mathrm{gb}},i-1}}}\right]\left(F^{\mathrm{eq}}_{\alpha,i-1}\right)\left(F_{\beta,i-2}\right) + F_{\alpha_{\mathrm{gb}},i-1} \end{aligned} \tag{8}$$

$$\begin{aligned} F_{\alpha_{\mathrm{w}},i} &= \Delta F_{\alpha_{\mathrm{w}},i-1} + F_{\alpha_{\mathrm{w}},i-1} \\ &= \left[1 - e^{-k_{\alpha_{\mathrm{w}},i}\left(t^{\mathrm{eq}}_{\alpha_{\mathrm{w}},i}+\Delta t\right)^{n_{\alpha_{\mathrm{w}},i}}}\right]\left(F^{\mathrm{eq}}_{\alpha,i}\right)\left(F_{\beta,i-1}\right) \\ &\quad - \left[1 - e^{-k_{\alpha_{\mathrm{w}},i-1}\left(t^{\mathrm{eq}}_{\alpha_{w},i-1}+\Delta t\right)^{n_{\alpha_{\mathrm{w}},i-1}}}\right]\left(F^{\mathrm{eq}}_{\alpha,i-1}\right)\left(F_{\beta,i-2}\right) + F_{\alpha_{\mathrm{w}},i-1} \end{aligned} \tag{9}$$

where the equilibrium transformation time for α_{gb} and α_{w} is expressed as:

$$t^{\mathrm{eq}}_{\alpha_{\mathrm{gb}},i} = \left[-\ln\left(1 - \left(1 - e^{-k_{\alpha_{\mathrm{gb}},i-1}\left(t^{\mathrm{eq}}_{\alpha_{\mathrm{gb}},i-1}+\Delta t\right)^{n_{\alpha_{\mathrm{gb}},i-1}}}\right)\right)/k_{\alpha_{\mathrm{gb}},i}\right]^{1/n_{\alpha_{\mathrm{gb}},i-1}} \tag{10}$$

$$t_{\alpha_{w},i}^{eq}=\left[-\ln\left(1-\left(1-e^{-k_{\alpha_{w},i-1}\left(t_{\alpha_{gb},i-1}^{eq}+\Delta t\right)^{n_{\alpha_{w},i-1}}}\right)\right)/k_{\alpha_{w},i}\right]^{1/n_{\alpha_{w},i-1}} \quad (11)$$

230

231 In order to predict the grain size for different phases, grain coarsening kinetics [51, 52] was adopted
232 to describe the evolution of α lath width and β grain size, as follows:

$$\bar{D}_i^c-\bar{D}_0^c=k_0\exp(-\frac{Q}{RT})t \quad (12)$$

233 where c is coarsening exponent, negatively related to grain growth rate, $\bar{D}_i$ is average size of grains
234 after coarsening, $\bar{D}_0$ is initial average grain size, k_0 is kinetic constant, Q is activation energy, taken
235 as 97 kJ/mol for Ti-6Al-4V [51], R is the gas constant, T is absolute temperature during heat treatment
236 and t is holding time. For α lath length, to account for constraint by β grain boundaries, a correction
237 pre-factor is defined as 0.2, i.e. α lath length is approximately one fifth of the β grain size.

238

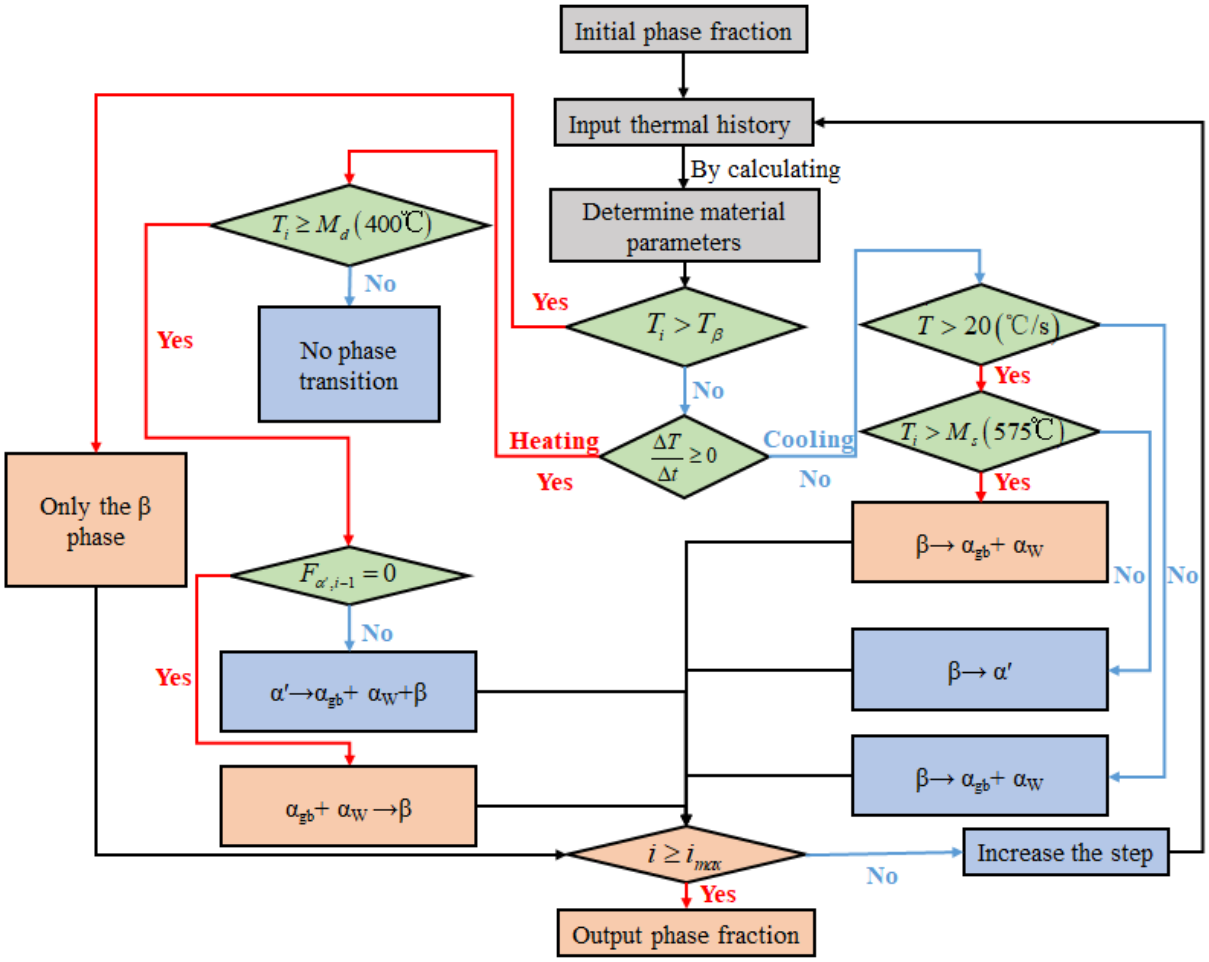

239

240 Figure 7. Flowchart of SSPT mechanisms during post-build heat treatment of PBF-LB Ti-6Al-4V.

241

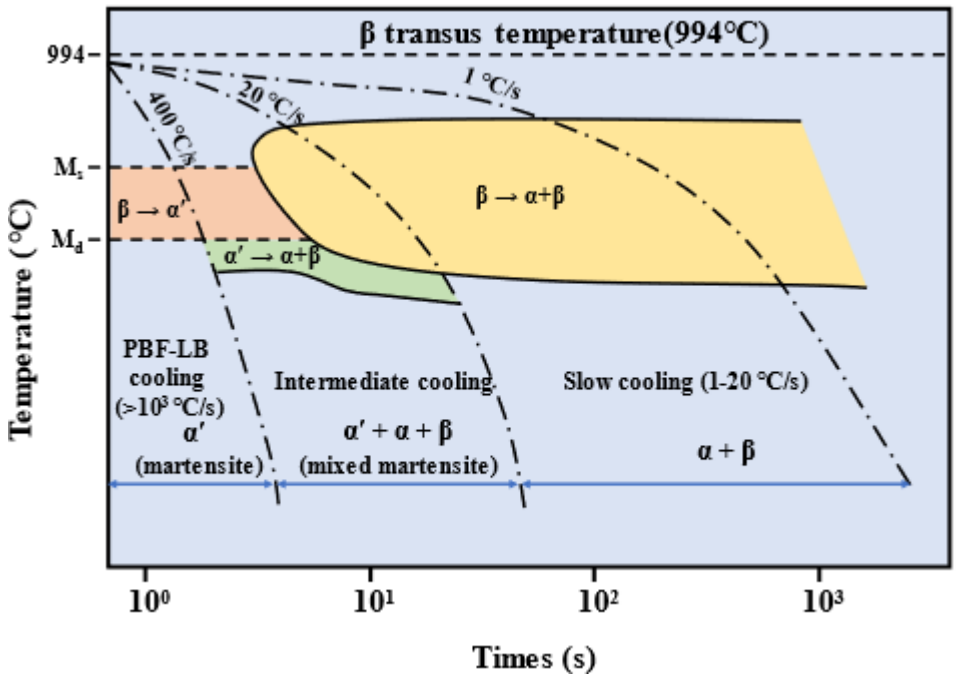

Figure 8. Continuous cooling transformation (CCT) curve of titanium alloy [9].

Based on these predicted key microstructure variables (i.e. phase fractions and grain sizes), our physically-based yield strength model is also implemented here to link microstructure to properties. The model is developed based on two assumptions: (i) assumption of iso-strain for all phases within the aggregate and (ii) the yield strength consists of a long-range athermal stress σ_{LR} and a short-range friction stress σ_{SR}. The formulation is expressed as:

$$\sigma_{\mathrm{y}} = \sum_{i} \left(\sigma_{\mathrm{LR},i} + \sigma_{\mathrm{SR},i}\right) F_i \qquad i = \alpha, \beta \text{ or } \alpha' \tag{13}$$

where σ_{y} is calculated yield strength and F_i is volume phase fraction obtained from the SSPT model. σ_{LR} is formulated as the sum of grain boundary hardening and forest stress, as:

$$\sigma_{\mathrm{LR},i} = \sigma_{\mathrm{HP},i} + \sigma_{\mathrm{for},i} = \frac{k_{\mathrm{HP},i}}{\sqrt{D_i}} + M\alpha_\rho \mu_i b_i \sqrt{\rho_{0,i}} \tag{14}$$

where the Hall-Petch coefficient $k_{\mathrm{HP},i} = \alpha_{\mathrm{G}}\mu_i\sqrt{b_i}$, α_{G} is material constant accounts for dislocation-grain interactions, μ_i is temperature-dependent Young's modulus, b_i is magnitude of Burgers vector, D_i is equivalent grain size, M is the Taylor factor, α_ρ is material constant related to the hardening from forest dislocations, $\rho_{0,i}$ is the initial dislocation density varies for different phases.

Specifically, the high dislocation density of α′ is estimated based on martensitic lath structure [24] while the measured value for conventional Ti-6Al-4V is taken for α and β. σ_{SR} is calculated in terms of Peierls-Nabarro stress and solid solution strengthening contribution, as:

$$\sigma_{\mathrm{SR}} = \sum_{i} M\left(\tau_{\mathrm{PN},i} + \tau_{\mathrm{SS},i}\right) G_i(T, \dot{\varepsilon}) \qquad i = \alpha, \beta \text{ or } \alpha' \tag{15}$$

where τ_{PN} is the Peierls-Nabarro stress, formulated as:

$$\tau_{\mathrm{PN},i} = \frac{2\mu_i}{1-\nu} \exp\left(\frac{-2\pi}{1-\nu}\right) \tag{16}$$

where ν is Poisson's ratio. τ_{SS} is calculated considering different element content (x_j) and corresponding strengthening constant ($B_{i,j}$), as:

$$\tau_{\mathrm{ss},i} = \left(\sum_{j} B_{i,j}^{3/2} x_j\right)^{2/3} \tag{17}$$

where $B_{i,j}$ is related to the shear modulus and lattice parameter misfits between phase *i* and element *j*, which can be calculated based on our previous work [24]. $G_i(T, \dot{\varepsilon})$ in Eq. (15) is a normalized activation energy and formulated as a function of temperature and strain rate ($\dot{\varepsilon}$), as:

$$G_i(T, \dot{\varepsilon}) = \left(\frac{f_0 \mu_i {b_i}^3}{k_{\mathrm{B}} T \ln(\dot{\varepsilon}_{\mathrm{ref}}/\dot{\varepsilon})}\right)^n \tag{18}$$

where f_0 is activation energy factor, k_{B} is Boltzmann's constant, $\dot{\varepsilon}_{\mathrm{ref}}$ is reference strain rate and *n* is a material constant related to the shape of energy barriers. Further details of this yield strength model are given in previous work [24].

4. Results

4.1 Experimental results

4.1.1 Microstructure

OM is used to observe the microstructure of Ti-6Al-4V specimens after the different heat treatment processes. Figure 9 shows the OM images of samples after 500 ℃ for 2 h and 600 ℃ for 2 h heat treatments. Acicular α′ martensite is retained after 500 ℃-2h heat treatment whereas a slight decrease of which is observed in the 600℃-2 h sample. For higher heat treatment temperatures, as shown in Figure 10, using MIPAR software [41], β-phase fractions are measured and calculated as

15.81%, 19.04%, 20.13%, 26.36% and 37.01% for Ti-6Al-4V specimens after holding for 2 hours at 700℃, 750℃, 800℃, 850℃ and 900℃, respectively, and accompanied with subsequent furnace cooling. Only a small variation of β-phase fraction is observed within the specimens heat-treated between 700 ℃ to 800℃ (Figure 10 (a)-(c)) and the phases mainly consists of α and β, dissolved from the sub-stable martensitic α'. When the holding temperature is increased above 850 ℃, the β-phase fraction increases significantly, along with decrease of α-phase. At the same time, coarsening of α lath is clearly observed with increase of holding temperature. The α lath width changes from 1.27±0.15 μm at 700 °C to 1.45±0.09 μm at 800°C and 2.08±0.13 μm at 900°C. For a fixed temperature increment of 50 °C, the increment of α lath width is 0.08 μm between 700 and 750°C and increases to 0.38 μm between 850 and 900°C, highlighting more significant coarsening at temperatures higher than 850 ℃. The measured α lath width, along with other key measured microstructure variables (i.e. α lath length and β grain size) are listed in Table 3.

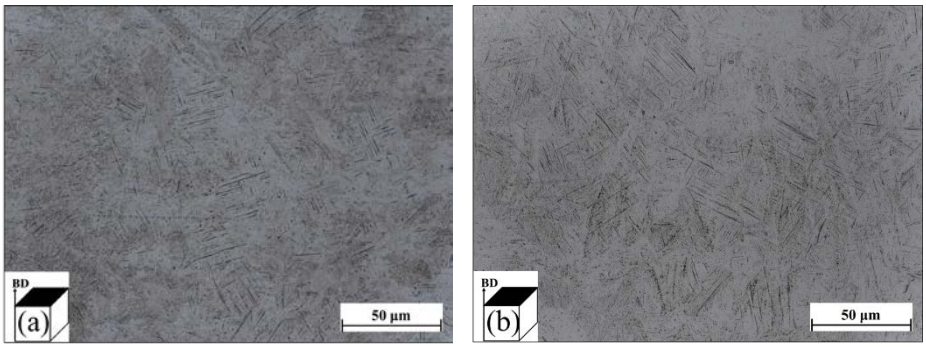

Figure 9. OM images of PBF-LB Ti-6Al-4V specimens heat-treated for 2 h at (a) 500℃; (b) 600℃.

Table 3. Key measured microstructure variables, including α lath width, length and β grain size.

Heat treatment temperature (℃)	α lath length μm	α lath width μm	β grain size μm
700	28	1.27	130
750	29	1.35	140
800	29	1.45	145
850	25	1.7	194
900	38	2.08	200

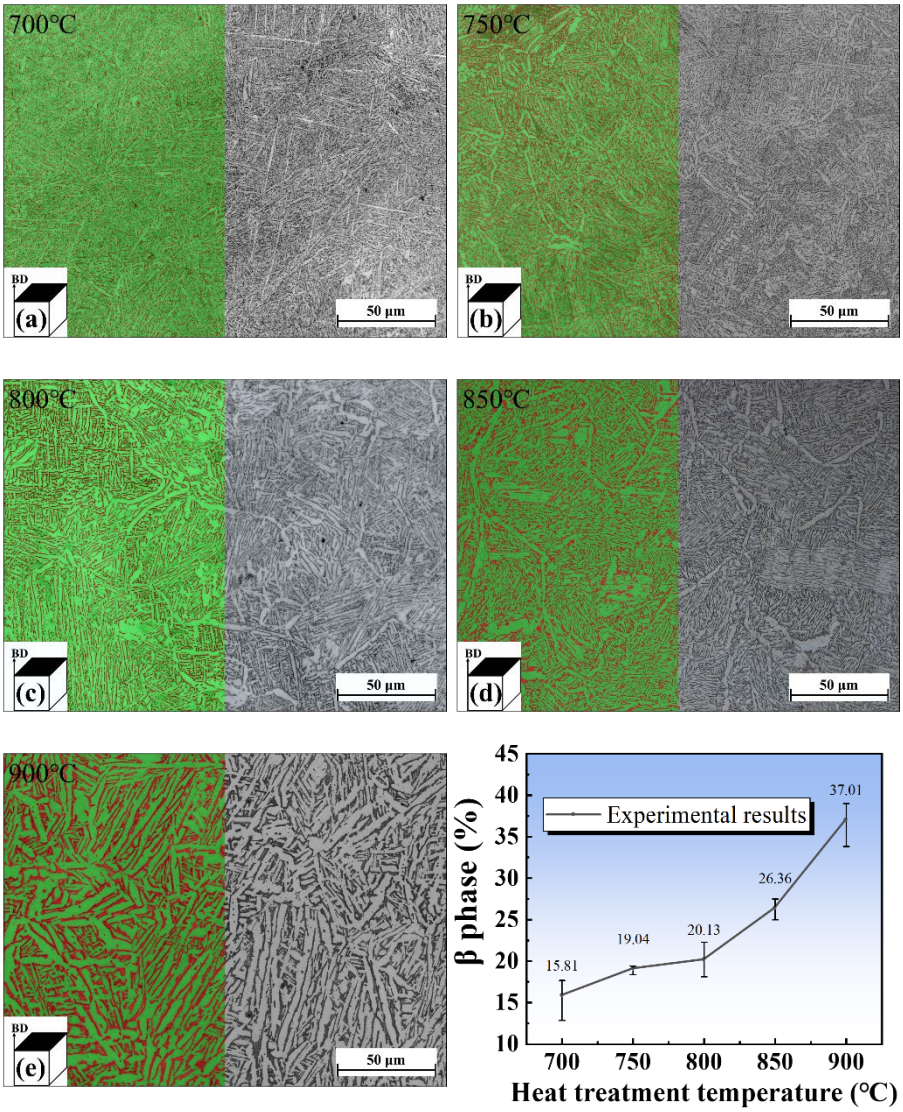

293 Figure 10. Metallographic characterization of the fraction of α-phase (green) and β-phase (red)
294 phases after heat-treatment at (a) 700℃; (b) 750℃; (c) 800℃; (d) 850℃; (e) 900℃; (f) Summary.
295
296 4.1.2 Tensile properties
297 The engineering stress-strain curves of PBF-LB Ti-6Al-4V after different heat treatments are
298 shown in Figure 11. Obvious necking and strain hardening stages are observed for both as-built and
299 heat-treated samples. The tensile properties including Young's modulus (E), yield strength (σ_y),
300 ultimate tensile strength (σ_{UTS}) and fracture elongation (δ), obtained from the tensile test curves, are
301 summarized in Table 4. In general, Young's modulus of the specimens is stable with respect to heat-
302 treatment (holding) temperature with all values higher than 106 GPa, indicating that the porosity
303 inherited from the manufacturing process is negligible. As per ASTM F2924-14 [53], minimum tensile

properties of PBF Ti-6Al-4V after thermal processing are as follows: should with σ_y, > 825 MPa, σ_{UTS} > 895 MPa and δ > 10%, respectively. The samples of 500 ℃ for 2 h and 600 ℃ for 2 h both have higher strength compared with the standard specification but are not qualified due to low elongation (<10%). With increasing holding temperature, the ductility of PBF-LB Ti-6Al-4V is significantly improved at the expense of strength. For example, the fracture elongation of the 900 ℃ for 2h sample is almost three times that of the 500 ℃ for 2h sample, while the yield strength drops about 30% from 1318 MPa to 949 MPa.

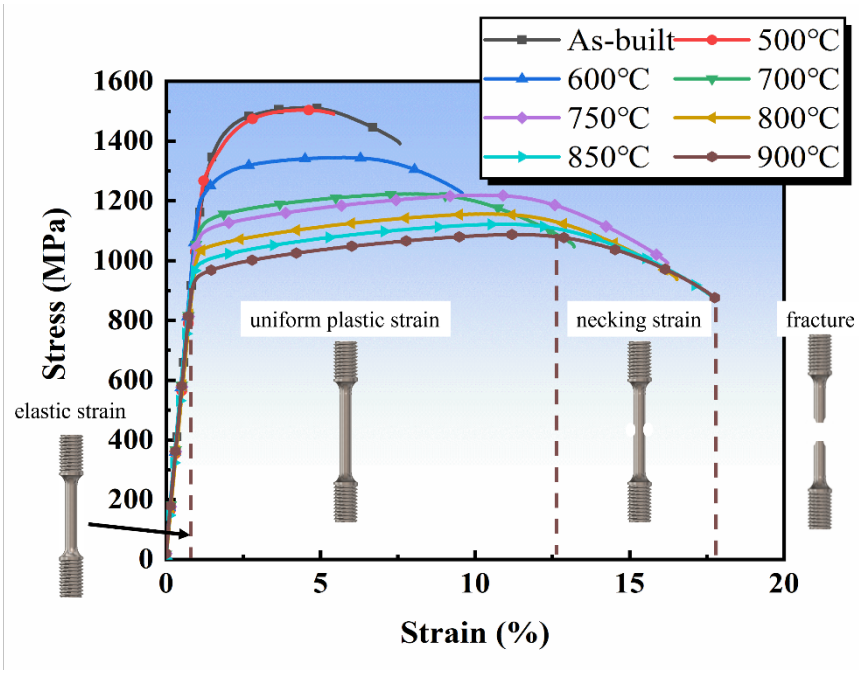

Figure 11. Effect of post-build heat-treatment (holding) temperature on room temperature monotonic tensile test response of PBF-LB Ti-6Al-4V after heat-treatment at different temperatures.

Table 4. Tensile properties of PBF-LB Ti-6Al-4V after heat treatment at different temperatures.

Heat-treatment temperature (℃)	Young's modulus (GPa)	Yield strength (MPa)	Ultimate tensile strength (MPa)	Fracture elongation (%)
As-built	111.2	1309	1510	7.56
500	106.7	1318	1504	5.42
600	115.3	1227	1345	9.59
700	111.5	1120	1223	13.21
750	109.8	1093	1220	16.24
800	106.6	1036	1156	16.53

850	115.7	987	1122	17.72
900	108.9	949	1088	17.77

316

317 **4.2 Model prediction results**

318 4.2.1 Predicted microstructure

319 Figure 12 shows the predicted phase fractions in PBF-LB Ti-6Al-4V with respect to different
320 heat treatment temperatures; corresponding material parameters are listed in Table 5. The β-phase
321 shows a gradual increase from 11.74% for the 500 ℃ sample to 37.6% for the 900 ℃ sample. At the
322 same time, α′ martensite phase fraction decreases quickly with increase of holding temperature and
323 is fully dissolved in the 700 ℃ sample. Increasing β-phase from 700 ℃ to 900 ℃ is attributed to the
324 subsequent α to β transformation. In addition, different α phase fractions are also shown in Figure 12.
325 α_w shows an increase from 500 ℃ to 700 ℃ due to the dissolution of α′ martensite while the
326 subsequent decrease is attributed to and contributes to the formation of β phase. α_{gb} phase fraction
327 can be neglected in all samples up to 800 ℃ and increases due to higher transformation rate at higher
328 temperatures. Figure 13 shows the comparison between experimental and predicted α lath width of
329 Ti-6Al-4V after heat treatment at the different temperatures. Coarsening of α lath width is successfully
330 predicted in terms of the consistent value of α lath width and the increased trend of coarsening rate
331 with respect to hold temperature.

332

333 Table 5. Material parameters of integrated PSP model for prediction of key microstructure variables
334 and yield strength.

Symbol	Unit	Phases	Value	Source
c	-	α, β	3	Fitted
$\bar{D}_0$	μm	α	1	Fitted
		β	100	Fitted
k_0	$\mu m^{-3}/s$	α	20	Calculated
		β	2×10^7	Calculated
α_G	-	α, α′, β	0.3	[54]
α_ρ	-	α, α′, β	0.5	[55]
M	-	α, α′, β	3.06	[56]
E	GPa	α	107	[57]
		α′	113	[58]
		β	105	Calculated

v	-	α, α′, β	0.34	[59]
μ	GPa	α	39.8	Calculated
		α′	43.3	Calculated
		β	39	[60]
b	nm	α, α′	0.295	[61]
		β	0.288	[60]
ρ_0	m^{-2}	α, β	4×10^{13}	[62]
f_0	-	-	0.42	Fitted
$\dot{\varepsilon}_{ref}$	s^{-1}	-	10^7	[63]
n	-	-	0.8	Fitted

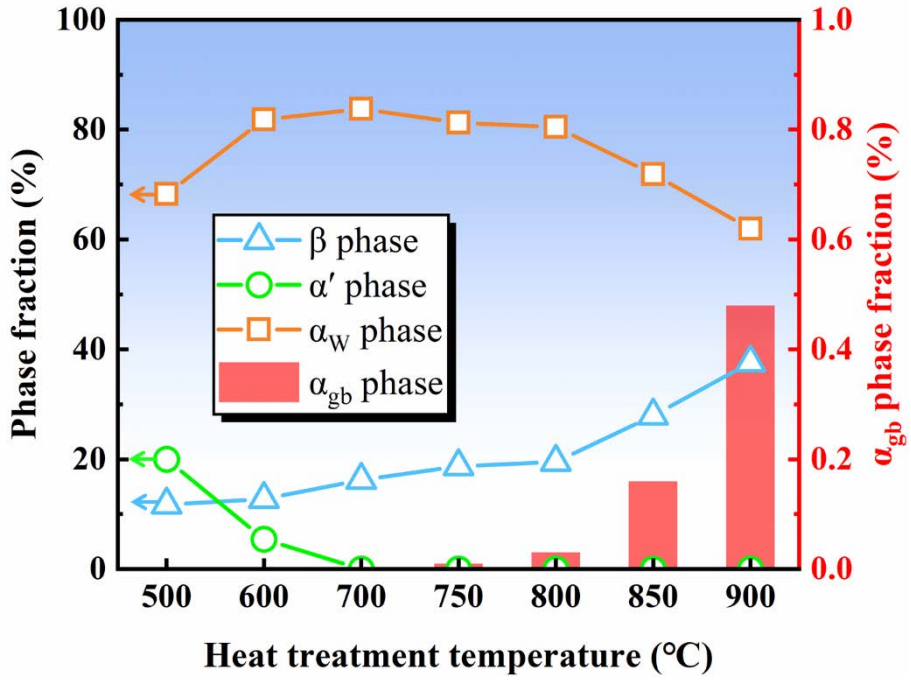

Figure 12. Predicted different phase fractions (β-phase and breakdown of α: α', α_w and α_{gb}) with respect to the heat treatment temperatures.

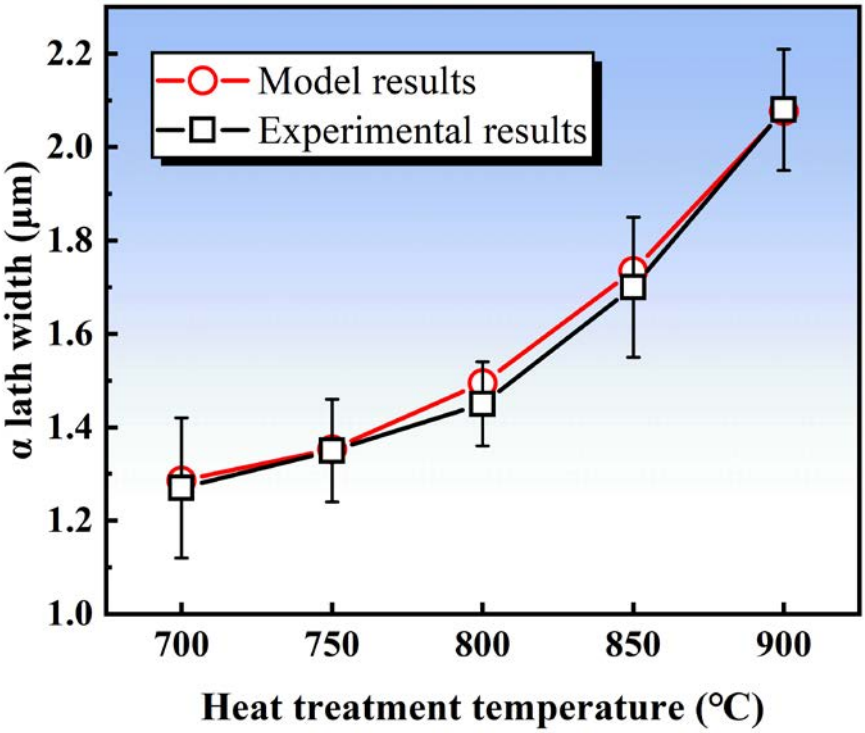

Figure 13. Comparison between experimental and predicted α lath width of Ti-6Al-4V after heat treatment at different temperatures.

4.2.2 Predicted yield strength

Figure 14 shows the predicted yield strength for PBF-LB Ti-6Al-4V after heat treatment at different temperatures using the integrated PSP model proposed in Section 3. Specifically, the predicted microstructure variables in Section 4.2.1 are used as input data for yield strength prediction. The downward trend of yield strength with respect to increasing heat treatment temperature is captured by the PSP model. The yield strength is predicted to decrease from 1486 MPa in the as-built state to 1174 MPa after 500 ℃ (2h) heat treatment with almost 21% decrease. Predicted variations among the samples from 700 ℃ to 800 ℃ is not significant while a nearly 33% decrease is predicted for the 900 ℃, compared to the as-built state, and this is about 100 MPa lower than that of the 700°C sample.

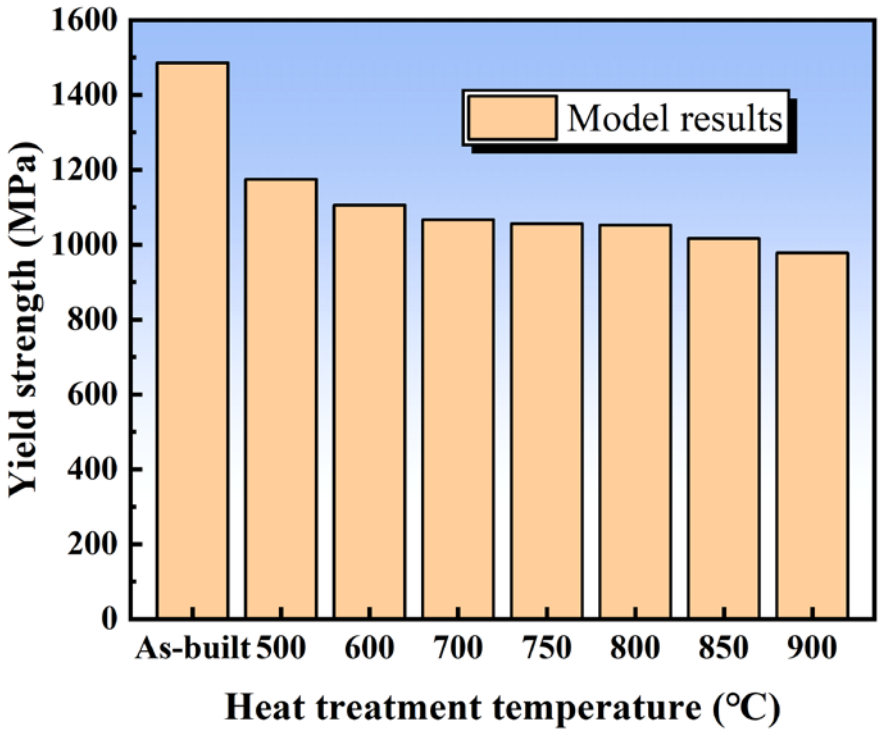

Figure 14. Predicted yield strength for PBF-LB Ti-6Al-4V after heat-treatment at different temperatures.

5. Discussion

5.1 Effect of different heat treatment temperatures on microstructure

Decomposition of α' martensite into α+β dual phase structure is the dominant SSPT mechanism during the post-build heat treatment of PBF-LB Ti-6Al-4V. The experimental results show that high temperature (>M_D) promotes coarsening of α′ martensite, leading to transformation of α′ martensite into lamellar α-phase. Combined with the predicted results, it is shown that heat treatment at 700 ℃ can completely eliminate α′ martensite. Subsequent coarsening of α-phase occurs during the holding process. When the temperature gets closer to the β transus temperature, β-phase is formed at the α-phase boundary, attributed to precipitation of vanadium as a eutectic stabilizer.

Since the phase fractions of α′ martensite and β-phase at 500 ℃ and 600 ℃ cannot be accurately measured by metallographic observation, the phase fraction of samples heat-treated from 700 ℃ to 900 ℃ are selected for verifying the model accuracy. As shown above, the α′ martensite transforms to α-phase completely after heat treatment above 700 ℃. The α-phase fraction, which is the sum of α_w and α_{gb}, as predicted by the model is compared with experimental results in Figure 15, showing that the prediction error is less than 2%.

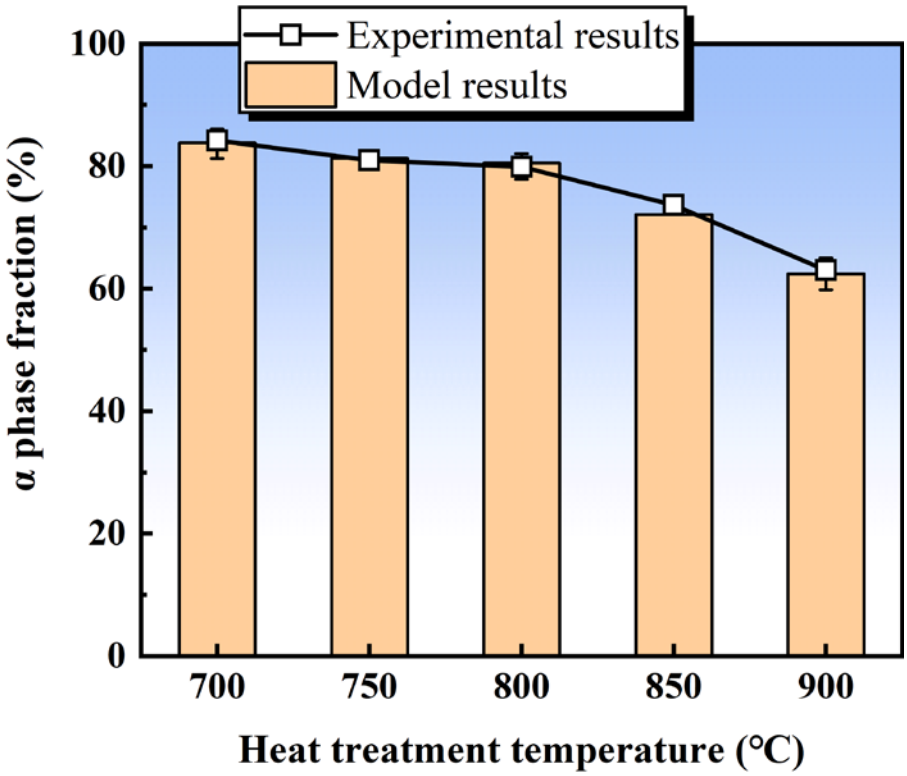

Figure 15. Comparison between experimentally measured and predicted α-phase fractions.

5.2 Effect of different heat treatment temperatures on tensile properties

Conventional Ti-6Al-4V has a dual phase structure with hard α-phase contributing to strength and soft β phase for ductility [64]. In PBF-LB Ti-6Al-4V, three phases co-exist, namely α, β and α′, during the post-heat treatment process. α′ is the hardest but is extremely brittle due to inherited high dislocation density from the fast cooling process of PBF-LB. Accompanied with the decomposition of α' martensite, ductility of PBF-LB Ti-6Al-4V increases significantly at the cost of reduced strength after heat treatment. In addition, formation of increased β-phase by increasing holding temperature further improves ductility, consistent with the findings of Kaschel et al. [65]. Figure 16 shows the strength contributions from different phases after heat treatment at different temperatures. Compared with the 500 ℃ heat-treated sample, heat treatment at 700 ℃ leads to 26.7% reduction of α′ martensite and the strength contribution from α′ martensite (313 MPa) is lost. At the same time, α-phase contributes a boost of 174 MPa with 15.5% increase of α-phase. Calculated results clearly show that α′ martensite offers a more significant strengthening effect than α-phase. Similarly, comparing the 700 ℃ to 900 ℃ heat-treated cases, the contribution of α-phase decreases by 245 MPa, with 20% reduction of phase fraction, while the 20% increase of β-phase only leads to 156 MPa contribution to yield strength, confirming that β-phase is the softest.

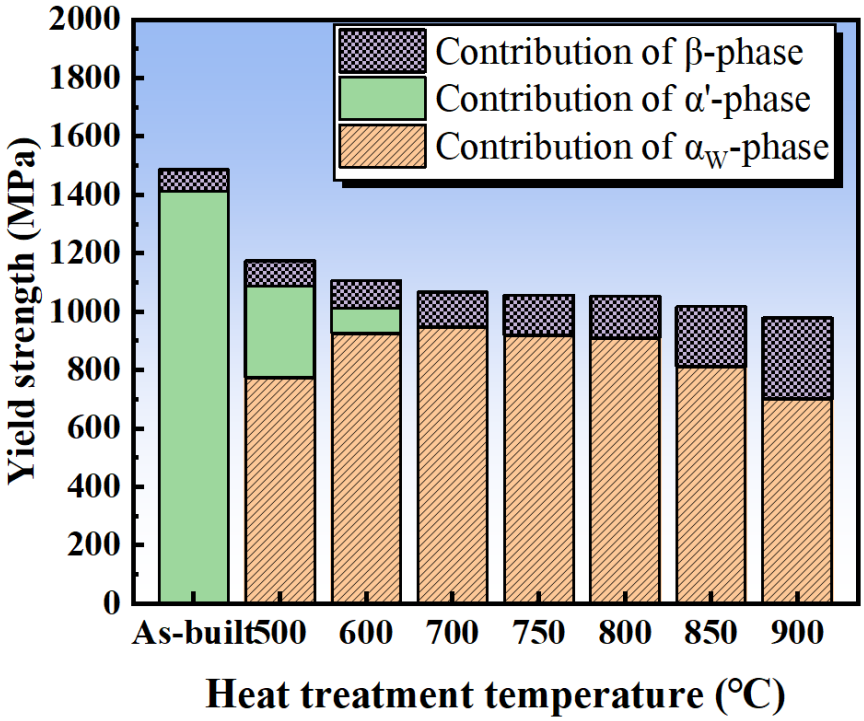

Figure 16. Predicted breakdown of the yield strength contribution from α, β and α′ phases after heat

treatments at different temperatures.

In order to validate the proposed PSP model, the predicted yield strength for different post-build heat treatment processes, based on predicted key microstructure variables (i.e. α lath width, length and β grain size), is compared with experimental monotonic tensile test results, as shown in Figure 17. The predictions for higher holding temperatures are more accurate, especially when α′ martensite is fully dissolved (i.e. > 700 ℃). the presence of the hard α′ martensite dominates the strength contribution of the three-phase system results in significant variation of yield strength prediction even for minor errors in predicted phase fraction. In addition, as α and α′-phase both have a HCP structure and share a similar lath-like morphology, it is difficult to accurately distinguish them from either X-ray powder diffraction (XRD) or microscopy. Thus, the prediction of individual α′-phase cannot be easily verified; this will be a focus of our future research.

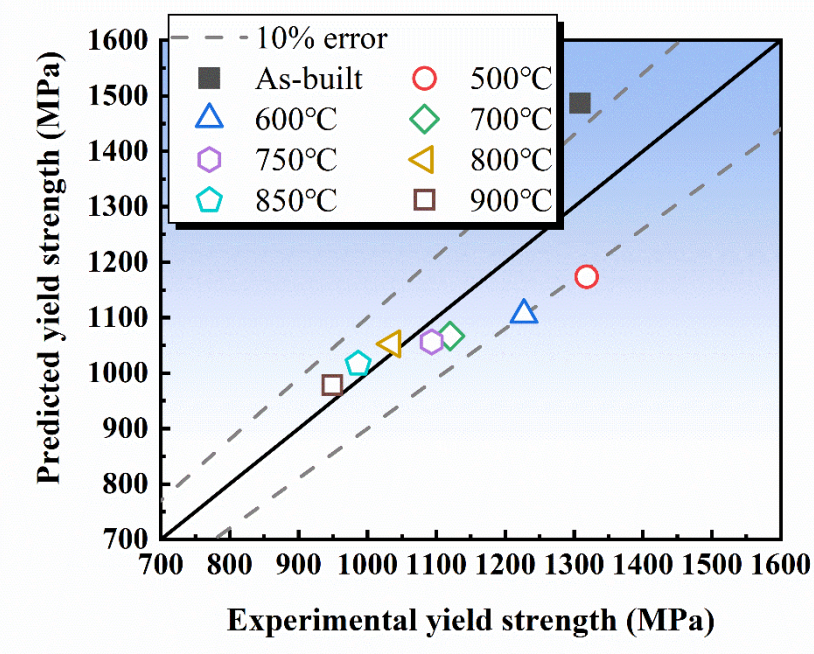

Figure 17. Comparison between experimental yield strength and predicted results.

6. Conclusion

In this paper, an integrated process-structure-property model for post-build heat treatment of PBF-LB Ti-6Al-4V is developed. The yield strength of samples with different heat treatment processes (e.g. holding temperatures) is successfully predicted via the accurate prediction of key microstructure variables such as α lath width, length and β grain size. Specific conclusions are as follows:

- The integrated process-structure-property model is validated against the experimental observations and published papers with acceptable accuracy.
- Low cooling rate effects of post-build heat treatment are captured in the present work to improve the prediction accuracy for phase fractions. The phase fraction of α′ martensite in the as-built state gradually reduces with increasing heat treatment temperature and no longer appears during slow cooling.
- β phase fraction is positively related to heat treatment temperature. Due to increased β phase fraction, the ductility of heat-treated PBF-LB Ti-6Al-4V is significantly improved at the cost of reduced strength. Tensile properties for the cases with heat treatment temperatures higher than 700 ℃ are shown to meet ASTM qualifaction standards for PBF-LB Ti-6Al-4V.
- The strength contributions of different phases is demonstrated. The relative strength contributions of α, β and α′ phases is rationalized by analyzing the strength variation due to phase change.
- The optimal heat treatment temperature, for post-build heat treatment of PBF-LB Ti-6Al-4V, can be determined inversely using the proposed process-structure-property model. The same approach could be adapted for other materials and processes.

Authorship

Jianxin Liu: Methodology, Software, Validation, Writing - original draft. **Xinyu Yang**: Conceptualization, Methodology, Software, Investigation, Writing - original draft, Writing - review & editing. **Xingzai Chai:** Software, Investigation. **Adrian Boccardo**: Methodology, Software. **Yefeng Chen**: Investigation, Writing - review & editing. **Xiaowei Wang**: Conceptualization, Investigation, Writing - review & editing, Project administration, Funding acquisition. **Seán B. Leen**:

Conceptualization, Methodology, Supervision, Writing - review & editing, Project administration, Funding acquisition. **Jianming Gong**: Supervision, Writing - review & editing, Project administration, Funding acquisition.

Acknowledgements

X. Yang gratefully acknowledges the financial support of the Structural Metal Alloys Program (grant no. A18B1b0061) of Agency for Science, Technology and Research (A*STAR), X. Wang gratefully acknowledges the financial support of the Key Project of University Natural Science Research in Jiangsu province (20KJA460002), Y. Chen acknowledges Postgraduate Research & Practice Innovation Program of Jiangsu Province (KYCX21_1119). X. Yang and S. Leen acknowledge the financial support of Science Foundation Ireland as part of I-Form Advanced Manufacturing Research Centre under grant number 16/RC/3872. For the purpose of Open Access, the author has applied a CC BY public copyright licence to any Author Accepted Manuscript version arising from this submission.

Data and code availability

The raw/processed data required to reproduce these findings cannot be shared at this time as the data also forms part of an ongoing study.

Conflicts of interest

The authors declare that they have no known competing financial interests or personal relationships that could have appeared to influence the work reported in this paper.

REFERENCES

1. Yap CY, Chua CK, Dong ZL, et al. Review of selective laser melting: Materials and applications. *Applied physics reviews* 2015; 2: 041101.
2. Barba D, Alabort C, Tang YT, et al. On the size and orientation effect in additive manufactured Ti-6Al-4V. *Materials & Design* 2020; 186: 108235.
3. Vrancken B, Thijs L, Kruth J-P, et al. Heat treatment of Ti6Al4V produced by Selective Laser Melting: Microstructure and mechanical properties. *Journal of Alloys and Compounds* 2012; 541: 177-185.
4. Alcisto J, Enriquez A, Garcia H, et al. Tensile Properties and Microstructures of Laser-Formed Ti-6Al-4V. *Journal of Materials Engineering and Performance* 2011; 20: 203-212.
5. Khorasani AM, Gibson I, Ghaderi A, et al. Investigation on the effect of heat treatment and process parameters on the tensile behaviour of SLM Ti-6Al-4V parts. *The International Journal of Advanced Manufacturing Technology* 2019; 101: 3183-3197.
6. Facchini L, Magalini E, Robotti P, et al. Ductility of a Ti-6Al-4V alloy produced by selective laser melting of prealloyed powders. *Rapid Prototyping Journal* 2010; 16: 450-459.
7. Li C-L, Hong J-K, Narayana P, et al. Realizing superior ductility of selective laser melted Ti-6Al-4V through a multi-step heat treatment. *Materials Science and Engineering: A* 2021; 799: 140367.
8. Olakanmi EO, Cochrane RF and Dalgarno KW. A review on selective laser sintering/melting (SLS/SLM) of aluminium alloy powders: Processing, microstructure, and properties. *Progress in Materials Science* 2015; 74: 401-477.
9. Sieniawski J, Ziaja W, Kubiak K, et al. *Microstructure and mechanical properties of high strength two-phase titanium alloys*. Rijeka: IntechOpen, 2013.
10. Karthikeyan T, Dasgupta A, Khatirkar R, et al. Effect of cooling rate on transformation texture and variant selection during β→ α transformation in Ti–5Ta–1.8 Nb alloy. *Materials Science and Engineering: A* 2010; 528: 549-558.
11. Gil F, Manero J, Ginebra M, et al. The effect of cooling rate on the cyclic deformation of β-annealed Ti–6Al–4V. *Materials Science and Engineering: A* 2003; 349: 150-155.
12. Davari N, Rostami A and Abbasi SM. Effects of annealing temperature and quenching medium on microstructure, mechanical properties as well as fatigue behavior of Ti-6Al-4V alloy. *Materials Science and Engineering: A* 2017; 683: 1-8.
13. Gil F, Ginebra M, Manero J, et al. Formation of α-Widmanstätten structure: effects of grain size and cooling rate on the Widmanstätten morphologies and on the mechanical properties in Ti6Al4V alloy. *Journal of Alloys and Compounds* 2001; 329: 142-152.
14. Kherrouba N, Bouabdallah M, Badji R, et al. Beta to alpha transformation kinetics and microstructure of Ti-6Al-4V alloy during continuous cooling. *Materials Chemistry and Physics* 2016; 181: 462-469.
15. Ahmed T and Rack H. Phase transformations during cooling in α+ β titanium alloys. *Materials Science and Engineering: A* 1998; 243: 206-211.
16. Zhang X-Y, Fang G, Leeflang S, et al. Effect of subtransus heat treatment on the microstructure and mechanical properties of additively manufactured Ti-6Al-4V alloy. *Journal of Alloys and Compounds* 2018; 735: 1562-1575.
17. de Formanoir C, Brulard A, Vivès S, et al. A strategy to improve the work-hardening behavior of Ti–6Al–4V parts produced by additive manufacturing. *Materials Research Letters* 2017; 5: 201-208.
18. Ma X, Li F, Li J, et al. Effect of heat treatment on the microstructure and micro-mechanical behavior of quenched Ti-6Al-4V alloy. *Journal of Materials Engineering and Performance* 2015; 24: 3761-3772.
19. Sahoo S and Chou K. Phase-field simulation of microstructure evolution of Ti–6Al–4V in electron beam additive manufacturing process. *Additive Manufacturing* 2016; 9: 14-24.
20. Zinovieva O, Zinoviev A and Ploshikhin V. Three-dimensional modeling of the microstructure evolution during metal

additive manufacturing. *Computational Materials Science* 2018; 141: 207-220.
21. De Baere D, Mohanty S and Hattel JH. Microstructural modelling of above β-transus heat treatment of additively manufactured Ti-6Al-4V using cellular automata. *Materials Today Communications* 2020; 24: 101031.
22. Yang X, Barrett RA, Tong M, et al. Towards a process-structure model for Ti-6Al-4V during additive manufacturing. *Journal of Manufacturing Processes* 2021; 61: 428-439.
23. Yang X, Barrett RA, Tong M, et al. Prediction of Microstructure Evolution for Additive Manufacturing of Ti-6Al-4V. *Procedia Manufacturing* 2020; 47: 1178-1183.
24. Yang X, Barrett RA, Harrison NM, et al. A physically-based structure-property model for additively manufactured Ti-6Al-4V. *Materials & Design* 2021; 205: 109709.
25. Yang X, Wang X, Brochu M, et al. Understanding orientation-dependent plasticity in laser beam powder bed fusion stainless steel through crystal plasticity modelling. *Materials Science and Engineering: A* 2022; 852: 143682.
26. Tang H, Huang H, Liu C, et al. Multi-Scale modelling of structure-property relationship in additively manufactured metallic materials. *International Journal of Mechanical Sciences* 2021; 194: 106185.
27. Tu Y, Liu Z, Carneiro L, et al. Towards an instant structure-property prediction quality control tool for additive manufactured steel using a crystal plasticity trained deep learning surrogate. *Materials & Design* 2022; 213: 110345.
28. Cao M, Liu Y and Dunne FPE. A crystal plasticity approach to understand fatigue response with respect to pores in additive manufactured aluminium alloys. *International Journal of Fatigue* 2022; 161: 106917.
29. Liu PW, Wang Z, Xiao YH, et al. Integration of phase-field model and crystal plasticity for the prediction of process-structure-property relation of additively manufactured metallic materials. *International Journal of Plasticity* 2020; 128: 102670.
30. Herriott C, Li X, Kouraytem N, et al. A multi-scale, multi-physics modeling framework to predict spatial variation of properties in additive-manufactured metals. *Modelling and Simulation in Materials Science and Engineering* 2019; 27: 025009.
31. Pilgar CM, Fernandez AM, Lucarini S, et al. Effect of printing direction and thickness on the mechanical behavior of SLM fabricated Hastelloy-X. *International Journal of Plasticity* 2022; 153: 103250.
32. Estrin Y, Tóth LS, Molinari A, et al. A dislocation-based model for all hardening stages in large strain deformation. *Acta Materialia* 1998; 46: 5509-5522.
33. Barrett RA, O'Donoghue PE and Leen SB. A physically-based constitutive model for high temperature microstructural degradation under cyclic deformation. *International Journal of Fatigue* 2017; 100: 388-406.
34. Barrett RA, O'Donoghue PE and Leen SB. A physically-based high temperature yield strength model for 9Cr steels. *Materials Science and Engineering: A* 2018; 730: 410-424.
35. Kelly SM. *Thermal and microstructure modeling of metal deposition processes with application to Ti-6Al-4V*. Virginia Tech, 2004.
36. Krakhmalev P, Fredriksson G, Yadroitsava I, et al. Deformation behavior and microstructure of Ti6Al4V manufactured by SLM. *Physics Procedia* 2016; 83: 778-788.
37. Mur FG, Rodríguez D and Planell J. Influence of tempering temperature and time on the α′-Ti-6Al-4V martensite. *Journal of alloys and compounds* 1996; 234: 287-289.
38. Welsch G, Boyer R and Collings E. *Materials properties handbook: titanium alloys*. ASM international: The Materials Information Society, 1993.
39. Crespo A. *Modelling of heat transfer and phase transformations in the rapid manufacturing of titanium components*. InTech, 2011.
40. Wang K, Meng M and Wang H. Effect of heat treatment and laser multi-track overlapping on microstructure of a laser melting deposition TC18 titanium alloy. *Infrared and Laser Engineering* 2010; 39: 521-525.
41. Sosa JM, Huber DE, Welk B, et al. Development and application of MIPAR™: a novel software package for two- and

549 three-dimensional microstructural characterization. *Integrating Materials and Manufacturing Innovation* 2014; 3: 123-
550 140.
551 42. Sosa J, Sul P and Small L. AUTOMATED MICROGRAPH ANALYSIS ENABLES PIONEERING R&D: Advances
552 in software algorithms and design enable automation of microstructure image analysis, leading to cost savings,
553 reduction in measurement variability, and access to important metrics. *Advanced Materials & Processes* 2019; 177:
554 16-22.
555 43. Kolmogorov A. On the static theory of crystallization in metals. *Bull Acad Sci USSR, Phys Ser* 1937; 1: 335.
556 44. Avrami M. Kinetics of phase change. I General theory. *The Journal of chemical physics* 1939; 7: 1103-1112.
557 45. Avrami M. Kinetics of phase change. II transformation-time relations for random distribution of nuclei. *The Journal*
558 *of chemical physics* 1940; 8: 212-224.
559 46. William J and Mehl R. Reaction kinetics in processes of nucleation and growth. *Trans Metall Soc AIME* 1939; 135:
560 416-442.
561 47. Murgau CC, Pederson R and Lindgren L-E. A model for Ti–6Al–4V microstructure evolution for arbitrary temperature
562 changes. *Modelling and Simulation in Materials Science and Engineering* 2012; 20: 055006.
563 48. Malinov S, Markovsky P, Sha W, et al. Resistivity study and computer modelling of the isothermal transformation
564 kinetics of Ti–6Al–4V and Ti–6Al–2Sn–4Zr–2Mo–0.08 Si alloys. *Journal of alloys and Compounds* 2001; 314: 181-
565 192.
566 49. Liu J, Zhang K, Yang Y, et al. Grain boundary α-phase precipitation and coarsening: Comparing laser powder bed
567 fusion with as-cast Ti-6Al-4V. *Scripta Materialia* 2022; 207: 114261.
568 50. Xu J, Zeng W, Zhao Y, et al. Influence of cooling rate following heat treatment on microstructure and phase
569 transformation for a two-phase alloy. *Journal of Alloys and Compounds* 2016; 688: 301-309.
570 51. Gil F and Planell J. Behaviour of normal grain growth kinetics in single phase titanium and titanium alloys. *Materials*
571 *Science and Engineering: A* 2000; 283: 17-24.
572 52. Gordillo M, Bedard B, Watson T, et al. Effect of heat-treatment on phase stability and grain coarsening in a powder-
573 processed Al–Ni–Co–Zr–Y alloy. *Journal of Materials Science* 2014; 49: 5866-5877.
574 53. Standard A. Specification for Additive Manufacturing Titanium-6 Aluminum-4 Vanadium with Powder Bed Fusion.
575 *ASTM International: West Conshohocken, PA, USA* 2014
576 54. Cordero ZC, Knight BE and Schuh CA. Six decades of the Hall–Petch effect – a survey of grain-size strengthening
577 studies on pure metals. *International Materials Reviews* 2016; 61: 495-512.
578 55. Ding R and Guo ZX. Microstructural evolution of a Ti–6Al–4V alloy during β-phase processing: experimental and
579 simulative investigations. *Materials Science and Engineering: A* 2004; 365: 172-179.
580 56. Stoller RE and Zinkle SJ. On the relationship between uniaxial yield strength and resolved shear stress in
581 polycrystalline materials. *Journal of Nuclear Materials* 2000; 283-287: 349-352.
582 57. ASME. ASME B31. 1,ASME Code for Power Piping. *The American Society of Mechanical Engineers: New York, NY,*
583 *USA* 2018
584 58. Attar H, Löber L, Funk A, et al. Mechanical behavior of porous commercially pure Ti and Ti–TiB composite materials
585 manufactured by selective laser melting. *Materials Science and Engineering: A* 2015; 625: 350-356.
586 59. Denlinger ER. *Thermo-mechanical model development and experimental validation for metallic parts in additive*
587 *manufacturing*. The Pennsylvania State University, 2015.
588 60. Zhao G-H, Liang XZ, Kim B, et al. Modelling strengthening mechanisms in beta-type Ti alloys. *Materials Science*
589 *and Engineering: A* 2019; 756: 156-160.
590 61. Frost H and Ashby M. *Deformation-mechanism maps: The plasticity and creep of metals and ceramics*. Pergamon
591 Press: Oxford, 1982.
592 62. Murr LE, Quinones SA, Gaytan SM, et al. Microstructure and mechanical behavior of Ti–6Al–4V produced by rapid-

layer manufacturing, for biomedical applications. *Journal of the Mechanical Behavior of Biomedical Materials* 2009; 2: 20-32.

63. Galindo-Fernández MA, Mumtaz K, Rivera-Díaz-del-Castillo PEJ, et al. A microstructure sensitive model for deformation of Ti-6Al-4V describing Cast-and-Wrought and Additive Manufacturing morphologies. *Materials & Design* 2018; 160: 350-362.

64. Hémery S, Nizou P and Villechaise P. In situ SEM investigation of slip transfer in Ti-6Al-4V: Effect of applied stress. *Materials Science and Engineering: A* 2018; 709: 277-284.

65. Kaschel FR, Vijayaraghavan RK, McNally PJ, et al. In-situ XRD study on the effects of stress relaxation and phase transformation heat treatments on mechanical and microstructural behaviour of additively manufactured Ti-6Al-4V. *Materials Science and Engineering: A* 2021; 819: 141534.